Direct 4D Parametric Imaging in Dynamic Myocardial Perfusion PET

Arman Rahmim[1,2*], Jing Tang[3], and Hassan Mohy-ud-Din[1,2]

1. Department of Radiology, Johns Hopkins University, USA.
2. Department of Electrical & Computer Engineering, Johns Hopkins University, USA.
3. Department of Electrical & Computer Engineering, Oakland University, USA.

Article info:
Received: June 22 2013
Accepted: August 15 2013

Keywords:
Myocardial perfusion,
PET,
4D reconstruction,
Optimization transfer.

ABSTRACT

Purpose: Dynamic myocardial perfusion (MP) PET imaging followed by tracer kinetic modeling allows quantification of myocardial blood flow, thus enabling computation of the coronary flow reserve, with considerable clinical potentials. Nonetheless, utilization of short dynamic frames can lead to noisy flow estimates, an issue that is further amplified in parametric imaging at the voxel level. Our purpose is to utilize an enhanced image reconstruction framework to better address this issue.

Methods: We implemented a novel 4D reconstruction scheme to directly estimate MP parametric images from the measured dynamic datasets. This included formulation of a 4D log-likelihood objective function relating the kinetic parameters to the projection datasets, and implementing numerical methods to optimize the objective function. We also utilized the technique of optimization transfer to enable more convenient and reliable parametric imaging. We simulated MP Rb-82 PET projection datasets based on the XCAT phantom utilizing patient-based time activity curves for the various organs and clinically realistic noise levels, followed by noise vs. bias analysis.

Results: The proposed direct 4D methodology was shown to outperform conventional indirect parametric imaging, reducing noise by over 50% (matched bias), with further reductions of 15% in noise and a factor of five speed-up when optimization transfer was additionally utilized.

Conclusion: Direct 4D PET image reconstruction is a viable and very promising approach towards robust parametric MP PET imaging at the individual voxel level.

1. Introduction

Myocardial perfusion (MP) PET provides improved diagnostic quality, certainty, and accuracy over conventional MP SPECT imaging [1-5]. The prognostic value in predicting adverse cardiac outcomes has also been demonstrated in an increasing number of studies [6-8]. In particular, dynamic MP PET imaging followed by tracer kinetic analysis (e.g. compartmental modelling applied to Rb-82 [9-15]), provides a powerful mean to estimate the tracer transport rate K1, and subsequently myocardial blood flow (MBF) which when measured under rest and stress used to calculate the coronary flow reserve (CFR). The CFR has been shown to be related to the degree of coronary artery stenosis (CAS) [16]. It thus allows for non-invasive assessment of the functional importance of CAS and may aid identification of patients with either diffuse, nonocclusive luminal coronary artery narrowing or a balanced reduction in coronary artery blood flow (extensive multi-vessel coronary disease) [17, 18]. CFR has also been shown to be reduced as a function of various coronary risk factors before the onset of clinically overt disease (e.g. in asymptomatic men with a family history of coronary artery disease (CAD) and high-risk lipid profiles [19]). Degradation of CFR based on other risk factors (e.g. hyperlipidemia, diabetes, smoking), has also been shown, supporting the beneficial effects of risk-factor modifications and novel medical therapies [20-32]. Non-invasive MP quantification may, therefore, allow early detection of preclinical

**** Corresponding Author:***
Arman Rahmim, PhD
Department of Radiology, Johns Hopkins Medical Institutions, Baltimore, Maryland, USA.
Tel: +1 410 5028579
E-mail: arahmim1@jhmi.edu

atherosclerosis, providing an opportunity to modify risk factors or initiate treatment. These studies have contributed to a paradigm shift in the perception of CAD, away from a pure macroscopic view of luminal stenoses and toward an emphasis on microcirculation and endothelial function [33-35]. Specifically, in persons with angiographically normal arteries, CFR has been shown to be a marker of coronary microvascular dysfunction [36], which can represent a new therapeutic target. Overall, changes in CFR promise to be extremely useful in assessing the effectiveness of treatment [37, 38].

Nonetheless, notwithstanding the vast potentials of the dynamic MP PET modality, it has remained primarily limited to research, and remains to be widely adopted in clinical practice [18, 39]. In fact, dynamic MP PET imaging is specifically challenged by the presence of additional noise due to division of the data into shorter frames, ultimately adversely impacting absolute flow quantification. In the present work, we propose a direct 4D reconstruction framework applicable to dynamic MP PET imaging enabling significant reductions in noise, and in fact, enabling parametric imaging at the individual voxel level.

2. Proposed Cardiac Parametric Imaging Framework

Conventional dynamic MP PET imaging consists of reconstructing the individual data frames followed by compartmental analysis to estimate kinetic parameters. A novel alternative is to instead directly estimate the kinetic parameters from the dynamic datasets. This approach has been reviewed elsewhere [40-42], and has typically involved parametric imaging at the voxel level for brain studies, or at the ROI-level in some cardiac studies. The present work elaborates upon our efforts [43-45] to develop and evaluate direct parametric imaging for dynamic cardiac PET imaging.

2.1. The Kinetic Model

We consider the one-tissue compartmental model (Figure 1) as commonly invoked in the literature to model kinetics of Rb-82 [10, 12, 13, 15]:

$$\frac{dC_M(t)}{dt} = K_1 C_a(t) - k_2 C_M(t) \quad (1)$$

Where $C_a(t)$ and $C_M(t)$ are the concentrations of Rb-82 in the arterial blood and the myocardium, respectively. By measuring the concentration $C_{LV}(t)$ via a small region size in the center of the LV cavity, nearly complete recovery of the arterial input curve and minimal myocardial spillover can be achieved [46], allowing a non-invasive approach; i.e. $C_a(t) = C_{LV}(t)$. Furthermore, to address the contribution of blood in the myocardial measurements, one writes:

$$C(t) = FC_a(t) + (1-F)C_M(t) \quad (2)$$

where $C(t)$ is the measured concentration of the tracer in the myocardium, and F represents the total fractional blood volume, combining (a) spillover due to the partial volume effect from the blood pool into the myocardial region or voxel of interest as well as (b) the presence of arterial blood in the muscle. Solving the abovementioned two equations yields:

$$C(t) = FC_a(t) + (1-F)K_1 \exp(-k_2 t) * C_a(t) \quad (3)$$

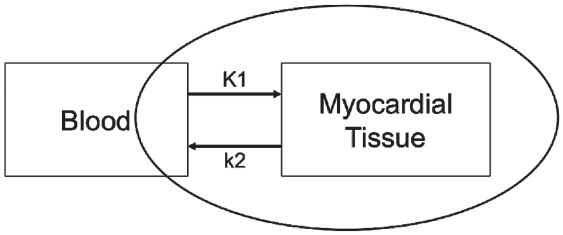

Figure 1. One-tissue compartmental model for kinetic modelling of Rb-82 MP PET imaging. The ellipse indicates the additional contribution of blood to the region or voxel of interest.

2.2. Direct 4D Problem Formulation and Numerical Optimization

To formulate the 4D problem, we next note that for a given parameter set K consisting of K_1, k_2, F across the voxels, the accumulated activity x_{jm} at any voxel j for any given dynamic frame m (spanning duration t_1 to t_2) can be written as:

$$x_{jm} = \int_{t_1}^{t_2} C_j(\tau)\, d\tau \quad (4)$$

Where $C_j(t)$ is given by (3) for any voxel j. This can then be used in connection with the system matrix $P = (p_{ij})_{I \times J}$ to arrive at the estimated projection-space data $\bar{y}_{im} = \sum_j p_{ij} x_{jm}$ for every LOR i. To achieve direct parametric estimation, we then note that the log-likelihood (L) function, to be maximized, is given by:

$$L(\mathbf{y}\,|\,\mathbf{K}) = \sum_{i,m} y_{im} \log \bar{y}_{im}(\mathbf{K}) - \bar{y}_{im}(\mathbf{K}) \qquad (5)$$

where the actual measured data are denoted by y_{im}.

We then apply numerical methods to iteratively search for kinetic parameters maximizing the L function, starting with an initial estimate $\mathrm{K}^{(0)}$ and arriving at subsequent updates to the parametric set. We considered preconditioned gradient ascent as we all as preconditioned conjugate gradient algorithms, implemented in C using numerical recipes, including ordered subsets and preconditioners. This is elaborated in Sec. 2.4.

2.3. Optimization Transfer

Aside from its nonconvex nature, numerical maximization of (5) is challenged by the computational burden of operations mapping the parametric image estimates to the projection-space at every iterative update. A powerful technique in optimization problems is to seek surrogate functions that can be more conveniently optimized, referred to as "optimization transfer" as explored in different contexts in the past [47-51]. Specifically, these techniques seek a surrogate function $Q(\mathbf{q};\mathbf{q}^n)$ depending on the current estimated parameter set of interest $\mathbf{q}^n$ in the log-likelihood function $L(\mathbf{y}\,|\,\mathbf{q}^n)$ such that $L(\mathbf{y}\,|\,\mathbf{q}) - Q(\mathbf{q};\mathbf{q}^n)$ has its minimum when $\mathbf{q} = \mathbf{q}^n$. Then, if we find the next estimate $\mathbf{q}^{n+1}$ that maximizes $Q(\mathbf{q};\mathbf{q}^n)$, i.e. $\mathbf{q}^{n+1} = \arg\max_{\mathbf{q}} Q(\mathbf{q};\mathbf{q}^n)$, it follows that $L(\mathbf{y}\,|\,\mathbf{q}^{n+1}) \geq L(\mathbf{y}\,|\,\mathbf{q}^n)$ thus guaranteeing improved estimation. This is because:

$$\begin{aligned} L(\mathbf{y}\,|\,\mathbf{q}^{n+1}) &= Q(\mathbf{q}^{n+1};\mathbf{q}^n) + \left(L(\mathbf{y}\,|\,\mathbf{q}^{n+1}) - Q(\mathbf{q}^{n+1};\mathbf{q}^n)\right) \\ &\geq Q(\mathbf{q}^n;\mathbf{q}^n) + \left(L(\mathbf{y}\,|\,\mathbf{q}^n) - Q(\mathbf{q}^n;\mathbf{q}^n)\right) \\ &= L(\mathbf{y}\,|\,\mathbf{q}^n) \end{aligned}$$

The surrogate functions are designed such that they are easier and/or less computationally intense to optimize than the original log-likelihood function. As such, for every update, the optimization is 'transferred' to the surrogate function, thus the name is optimization transfer. We also note that a very natural special case of the above condition is having a surrogate function that bounds the log-likelihood function from below everywhere, touching it at $\mathbf{q}^n$; i.e.

$$\begin{aligned} L(\mathbf{y}\,|\,\mathbf{q}) &\geq Q(\mathbf{q};\mathbf{q}^n) \\ L(\mathbf{y}\,|\,\mathbf{q}^n) &= Q(\mathbf{q}^n;\mathbf{q}^n) \end{aligned}$$

This is depicted in Figure 2.

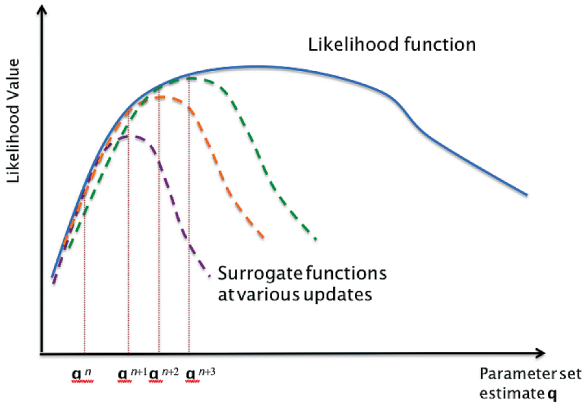

Figure 2. Optimization using surrogate functions that are iteratively constructed and maximized providing subsequent updates.

Wang and Qi applied the optimization transfer concept to direct parametric imaging in the case of linear kinetic models [52]. They also pursued the non-linear context developing a separable paraboloidal surrogate [53] and an EM surrogate [54]. The latter approach was shown to exhibit more favourable convergence properties, which we also use towards dynamic MP PET imaging as elaborated next.

In particular, the resulting surrogate function to the log-likelihood function (5) can be shown to be:

$$Q(\mathbf{K};\mathbf{K}^n) = \sum_j \left[\left(\sum_i p_{ij} \right) \sum_m \left(\hat{x}_{jm}^{EM}(\mathbf{K}^n) \log x_{jm}(\mathbf{K}) - x_{jm}(\mathbf{K}) \right) \right] \qquad (6)$$

where

$$\hat{x}_{jm}^{EM}(\mathbf{K}^n) = \frac{x_{jm}(\mathbf{K}^n)}{\sum_i p_{ij}} \sum_i \frac{p_{ij} y_{jm}}{\sum_q p_{iq} x_{qm}(\mathbf{K}^n)} \qquad (7)$$

is an EM update to the existing image estimate $x_{jm}(\mathbf{K}^n)$. An important observation is that the surrogate function (6) is separable in voxels, and thus its maximization can be conveniently carried out voxel-by-voxel:

$$\mathbf{K}^{n+1} = \arg\max_{\mathbf{K}} Q(\mathbf{K};\mathbf{K}^n) \qquad (8)$$

Overall, instead of performing direct parametric imaging via maximization of the log-likelihood (5), the alternative optimization transfer formulation (6), (7) and (8)

enables decoupling of the kinetic-parameter-to-image and image-to-sinogram relationships at each iteration, allowing more convenient and more frequent updates. Thus one starts with an initial estimate $K^{(0)}$ of the parameter set, followed by utilization of the sinogram data to produce $\lambda_j^{EM,m}$ according to (7), and subsequently using (6) and (8) to work conveniently in the image-space domain only, performing optimization of Q voxel-by-voxel, to arrive at the next update parameter set K, and onwards.

2.4. Ordered-Subsets Method and the Detailed Numerical Implementation

Analogous to the concept of ordered-subsets (OS) as utilized in standard OS-EM algorithms [55], it is possible to similarly expand both aforementioned formulations (schemes without and with optimization transfer). In particular, for every update, only an angular subset of the measured dynamic dataset is utilized, in order to speed up the computations.

To compare the performance of steepest ascent vs. conjugate gradient methods in the context of OS, we first simplify the numeric problem to the standard case of static image reconstruction. The standard EM algorithm can in fact be formulated as a fixed step-size special case of preconditioned steepest ascent (PSA), while PSA and preconditioned conjugate gradient (PCG) algorithms allow variable, optimal step-sizes for each new direction. To see this, we note that the standard log-likelihood function is given by:

$$L(\mathbf{y}\,|\,\mathbf{x}) = \sum_i y_i \log \bar{y}_i - \bar{y}_i \tag{9}$$

where

$$\bar{y}_i = \sum_j p_{ij} x_j \tag{10}$$

Furthermore, the EM algorithm maximizing the above log-likelihood function is given by [56, 57]:

$$x_j^{(t+1)} = \frac{x_j^{(t)}}{\sum_i p_{ij}} \sum_i \frac{p_{ij} y_i}{\sum_q p_{iq} x_q^{(t)}} \tag{11}$$

Where t denotes the iterative update number. It is easy to see [58-60] that the EM algorithm is effectively a fixed step-size special case of preconditioned gradient ascent: consider a preconditioner C_j and step-size α. Then, the update iteration is as follows:

$$x_j^{(t+1)} = x_j^{(t)} + \alpha C_j \frac{\partial L(\mathbf{y}\,|\,\mathbf{x})}{\partial x_j^{(t)}} \tag{12}$$

Noting that:

$$\frac{\partial L(\mathbf{y}\,|\,\mathbf{x})}{\partial x_i} = \sum_i \left(\frac{p_{ij} y_i}{\sum_q p_{iq} x_q} - p_{ij} \right) \tag{13}$$

It follows that (11) and (12) are equivalent if $\alpha = 1$ and the preconditioner is set as follows:

$$C_j = \frac{x_j^{(t)}}{\sum_i p_{ij}} \tag{14}$$

For our direct 4D parametric imaging framework (5), we utilized a general form somewhat similar to (12) but optimized with respect to the kinetic parameters K_j^p (p=1,2,3; where for a given voxel j, three parameters K_1, k_2, F_{LV} are to be estimated):

$$K_j^{p,(t+1)} = K_j^{p,(t)} + \alpha C_j^p \frac{\partial L(\mathbf{y}\,|\,K)}{\partial K_j^{p,(t)}} \tag{15}$$

With our preconditioners set to:

$$C_j^p = \frac{K_j^{p,(t)}}{\sum_i p_{ij}} \tag{16}$$

The numerical update algorithm then optimizes in each iteration for steepest ascent, thus arriving at PSA. We also implemented a PCG variant, involving the Fletcher-Reeves-Polak-Ribiere method [61]. The OS technique, commonly applied to achieve OS-EM, was then applied to result in OS-PSA and OS-PCG variants.

3. Experimental Design

3.1. Simulations

We generated myocardial perfusion Rb-82 PET datasets using the XCAT phantom [62], combined with analytic simulations, including the effects of attenuation and normalization. The geometry of the GE Discovery RX PET [63] was considered, including realistic average counts and noise levels based on clinical studies of five patients with healthy myocardia at the Johns Hopkins PET Center, as we also previously utilized in a different context [64]. Rb-82 PET patient organ time activity curves for the various organs in the field-of-view were acquired (Figure 3) and fitted to generate a set of kinetic parameters for the organs. The resulting para-

metric images (Figure 4) served as the basis, and reference truth, for the realistic simulations.

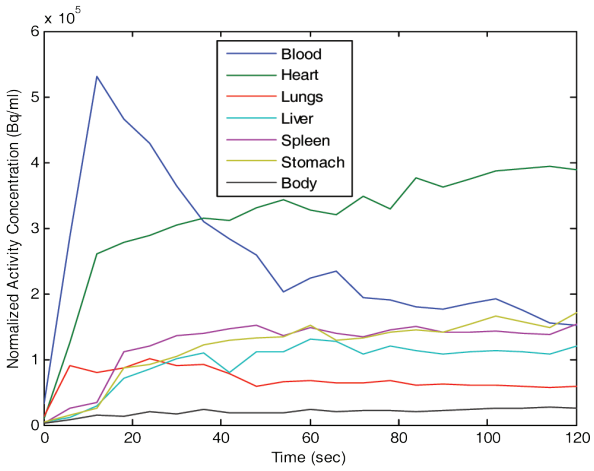

Figure 3. Average organ time activity curves from 5 patients with healthy myocardia.

Figure 4. A transaxial slice of the K1, k2, and FLV parametric images generated for the NCAT phantom, and used for subsequent simulations.

3.2. Quantitative Analysis

To track convergence of OS methods, we computed a metric, referred to as the asymptotic normalized log-likelihood difference (NLD), given by:

$$NLD(n) = \frac{L(\mathbf{y}\,|\,\hat{\mathbf{x}}) - L(\mathbf{y}\,|\,\mathbf{x}^{(n)})}{L(\mathbf{y}\,|\,\hat{\mathbf{x}}) - L(\mathbf{y}\,|\,\mathbf{x}^{(0)})} \qquad (17)$$

where $\hat{\mathbf{x}}$ denotes a reference image after substantial iterations (i.e. at near convergence). This enabled us to identify whether OS-PSA or OS-PCG is more appropriate as method of choice for numerical optimization (Sec. 4.1).

For quantitative assessment of the results, polar maps were created from the estimated K_1 values on the left ventricular myocardium. The polar maps were subdivided into 10 sub-regions as depicted in Figure 5, for additional regional quantitative analysis.

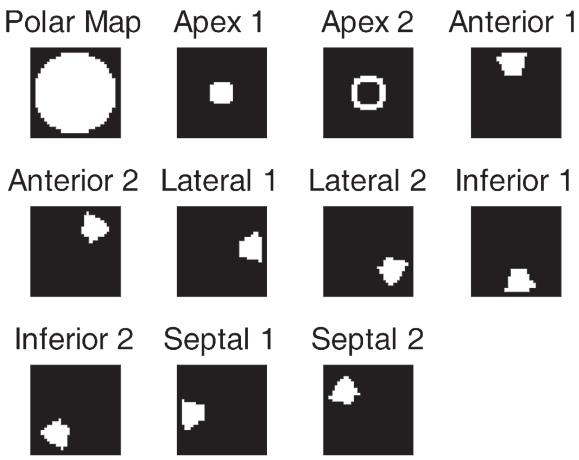

Figure 5. Masks to divide the polar map into different segments for analysis.

The three approaches of (i) conventional reconstruction followed by compartmental fitting, as well as direct 4D parametric imaging (ii) without and (iii) with optimization transfer, as elaborated in Sec. 2, were considered. Comparisons were performed using noise vs. bias trade-off curves as generated with increasing iterations into the reconstructions. This was performed for the entire LV myocardium, as well as the 10 segments shown above.

4. Results

4.1. Optimization Methods in the Context of OS

For our initial studies in the case of static imaging, PSA and PCG algorithms were seen to converge as fast as the EM algorithm, while producing overlapping noise vs. bias trade-off curves (not shown). However, when utilizing subsets, the OS-PCG algorithm was seen to converge relatively poorly relative to both OS-EM and OS-PSA algorithms, as shown in Figure 6 (normalized likelihood difference, computed by (17), was seen to be larger by factors of 1.8 and 2.5 respectively). We attribute this to the fact that while the PCG technique has theoretical advantages compared to moving in the direction of steepest ascent, this effect disappears for OS data due to inherent inconsistencies between the data subsets. We thus concluded that usage of the PCG algorithm in the OS context is not recommended, while OS-PSA and OS-EM algorithms pose more favorable

alternatives. In applications where the EM solution does not exist (e.g. non-linear 4D parametric imaging pursued in this work), usage of OS-PSA optimization is instead recommended, which is what we utilized in the rest of this work.

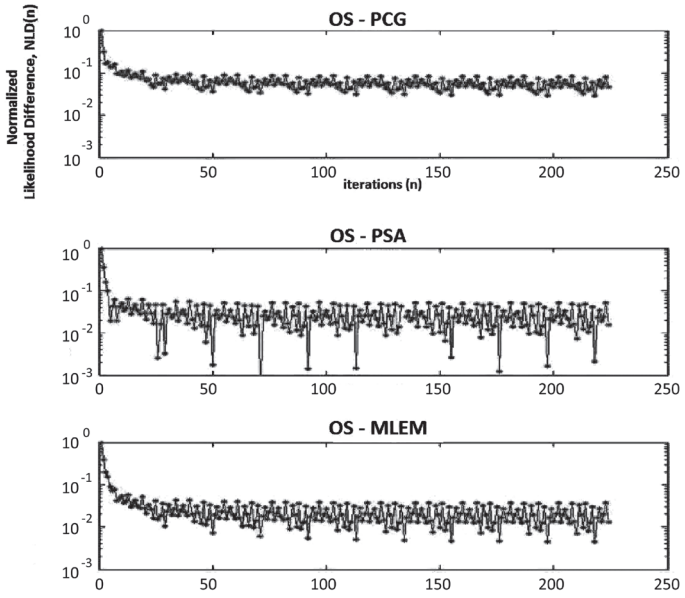

Figure 6. In the context of OS, PCG is seen to converge relatively slowly compared to the PSA and EM counterparts.

4.2 Direct 4D Parametric Imaging without Optimization Transfer

Analysis of noise (normalized standard deviation) vs. bias (normalized mean squared error) trade-off curves, as generated by varying the iterations, revealed significant improvements for the proposed 4D method in the entire polar map and in all individual regions of interest (apex, anterior, lateral, inferior and septal) relative to conventional indirect parametric imaging, as seen

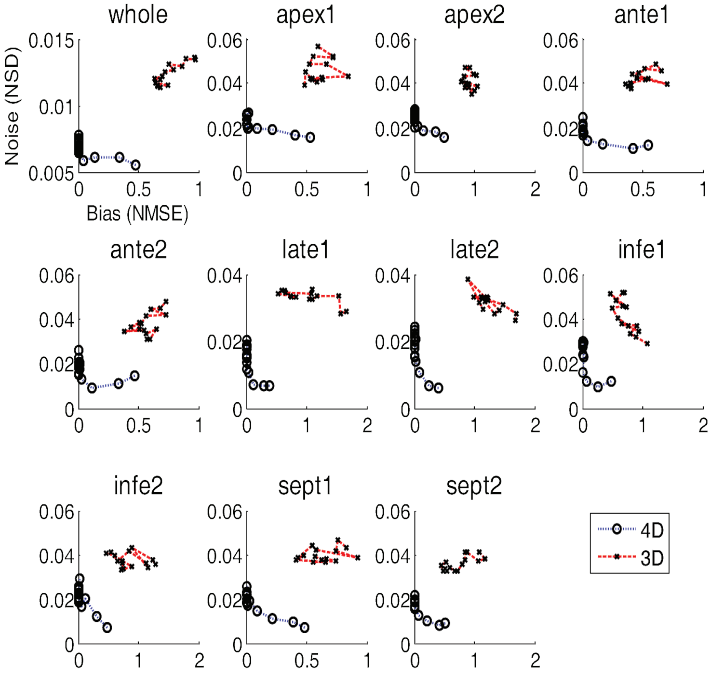

Figure 7. Noise vs. bias curves (generated by varying the iterations) for the entire K1 polar map and for the individual segments. The 4D direct reconstruction outperforms conventional compartmental fitting following reconstruction of individual frames.

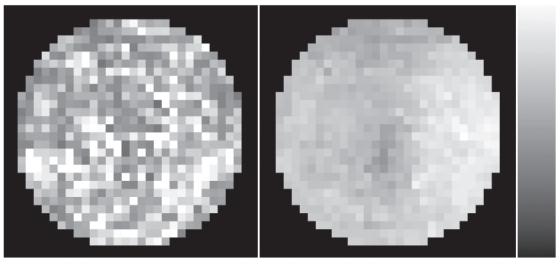

Figure 8. Polar maps with matched bias for (left) conventional indirect kinetic parameter estimation, and (right) proposed direct 4D parametric imaging. Clearly suppressed noise levels are observed.

in Figure 7. For visual inspection, Figure 8 shows the two polar maps which were picked in such a way to be quantitatively matched in terms of bias: clearly reduced noise levels are observed; in fact, the proposed 4D technique produced over 50% overall reduction in noise, with matched bias.

4.3. Direct 4D Parametric Imaging with Optimization Transfer

A significant factor-of-five improvement in computational efficiency was achieved for 4D parametric imaging utilizing optimization transfer compared to the 4D approach not utilizing optimization transfer. This is due to the decoupling between the sinogram and image space domains, as discussed in Sec. 2.3. Moreover, noise vs. bias trade-off analysis, as shown in Figure 9, revealed enhanced quantitatively performance for optimization transfer, as could also be detected via visual

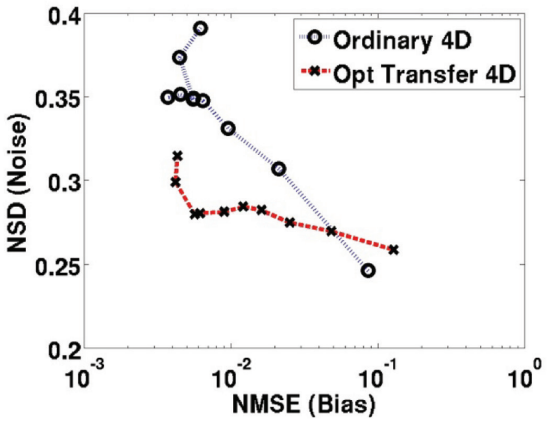

Figure 9. Noise vs. bias curves (generated by varying the iterations) for the entire K1 polar map. The approach utilizing optimization transfer is seen to perform favorably compared to the baseline direct 4D reconstruction methods.

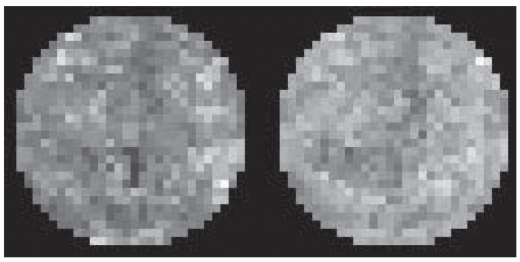

Figure 10. Polar maps obtained using direct 4D reconstruction (left) without and (right) with optimization transfer.

inspection (Figure 10): over 15% reduction in noise was obtained, with matched bias.

5. Discussion

5.1 Parameter Estimation Outside the Myocardium

An area of caution in direct parametric imaging is the inherent assumption that the compartmental model of interest is valid everywhere within the image. Otherwise, if the model is inaccurate outside a region of interest, errors can still be propagated to the region [65, 66], unlike the conventional indirect estimation framework where kinetic fitting is independently performed for each voxel or region of interest. In any case, in our context of Rb-82 MP PET, our preliminary analysis indicated that time activity curves outside the myocardium were appropriately fit using the standard one-tissue compartment model (no systematic residual errors). It is worth noting, at the same time, that we do not interpret the fits outside the myocardium, though Rb-82 has been proposed as a tracer with potential for renal blood flow imaging, including demonstration of appropriate fits in the kidney using the one-tissue compartmental model [67].

5.2 Addressing the Partial Volume Effect (PVE)

One presented issue in both static and dynamic imaging is PVE, which arises from the contributions of resolution degrading phenomena [68]. In the case of dynamic imaging, an attempt to address PVE has been through additional parameters in the kinetic modelling analysis [15, 69-74] (e.g. note that the fractional blood volume F as implemented in Sec. 2.1 is aimed, in part, to model the spillover from the blood pool to the myocardium). However, use of additional variable(s) can degrade estimation robustness. Other alternatives explored for cardiac imaging include post-reconstruction partial volume correction (PVC) [75-79] or reconstruction-based reso-

lution modelling [80-82]. In fact, in one explicit comparison by Nuyts et al. [75], PVC was seen to outperform the expanded kinetic modelling approach. A downside to direct 4D parametric estimation is that because individual images are not reconstructed, PVC cannot be applied as such to final reconstructed individual images; however, it is possible to investigate application of PVC to the final parametric image, though this is not an equivalent approach. By contrast, resolution modelling can be easily incorporated in the context of 4D image reconstruction. However, resolution modelling itself is an area that needs to be approached with caution, especially in the context of quantitative imaging [83] because even though it leads to improved resolution and contrast recovery (reduced quantitative bias) it can amplify variability (i.e. reduce reproducibility) for small regions of interest, and can lead to edge artifacts [84].

6. Summary

A direct 4D parametric imaging method was developed incorporating kinetic modeling within the reconstruction of dynamic cardiac PET data. With realistic simulations, we demonstrated improved quantitative performance of the proposed technique over conventional indirect quantification of myocardial blood flow following reconstruction of individual images. Optimization transfer via construction of an image-domain surrogate function was seen to notably enhance computational as well as quantitative performance of direct parametric image estimation.

Acknowledgment

This work was in part supported by the NIH grant 1S10RR023623 and the NSF grant ECCS 1228091. The authors wish to thank Dr. Bengel for helpful discussions, and Andy Crabb for computational support.

References

[1] Go, R.T., et al. (1990). A Prospective Comparison of Rubidium-82 PET and Thallium-201 SPECT Myocardial Perfusion Imaging Utilizing a Single Dipyridamole Stress in the Diagnosis of Coronary Artery Disease. J Nucl Med, 31(12), 1899-1905.

[2] Stewart, R.E., et al. (1991). Comparison of rubidium-82 positron emission tomography and thallium-201 SPECT imaging for detection of coronary artery disease. Am J Cardiol, 67(16), 1303-10.

[3] Machac, J. (2005). Cardiac positron emission tomography imaging. Semin Nucl Med, 35(1), 17-36.

[4] Bateman, T.M., et al. (2006). Diagnostic accuracy of rest/stress ECG-gated Rb-82 myocardial perfusion PET: comparison with ECG-gated Tc-99m sestamibi SPECT. J Nucl Cardiol, 13(1), 24-33.

[5] Sampson, U.K., et al. (2007). Diagnostic accuracy of rubidium-82 myocardial perfusion imaging with hybrid positron emission tomography/computed tomography in the detection of coronary artery disease. J Am Coll Cardiol, 49(10), 1052-8.

[6] Marwick, T.H., et al. (1997). Incremental value of rubidium-82 positron emission tomography for prognostic assessment of known or suspected coronary artery disease. Am J Cardiol, 80(7), 865-70.

[7] Yoshinaga, K., et al. (2006), What is the Prognostic Value of Myocardial Perfusion Imaging Using Rubidium-82 Positron Emission Tomography? J Am Coll Cardiol, 48(5), 1029-1039.

[8] Schenker, M.P., et al. (2008). Interrelation of coronary calcification, myocardial ischemia, and outcomes in patients with intermediate likelihood of coronary artery disease: a combined positron emission tomography/computed tomography study. Circulation, 117(13), 1693-700.

[9] Herrero, P., et al. (1992). Implementation and Evaluation of a 2-Compartment Model for Quantification of Myocardial Perfusion with Rb-82 and Positron Emission Tomography. Circulation Research, 70(3), 496-507.

[10] Coxson, P.G., et al. (1995). Variability and Reproducibility of Rb-82 Kinetic-Parameters in the Myocardium of the Anesthetized Canine. Journal of Nuclear Medicine, 36(2), 287-296.

[11] Yoshida, K., Mullani, N., and Gould, K.L. (1996). Coronary flow and flow reserve by PET simplified for clinical applications using rubidium-82 or nitrogen-13-ammonia. Journal of Nuclear Medicine, 37(10), 1701-1712.

[12] Coxson, P.G., Huesman, R.H. and Borland, L. (1997). Consequences of using a simplified kinetic model for dynamic PET data. Journal of Nuclear Medicine, 38(4), 660-667.

[13] Golanowski, L., et al. (2000). Variance and Covariance of 82Rb Kinetic Parameters: Computer Simulations and Dynamic PET Studies, in Proceedings of the 22nd Annual International Conference of the IEEE Engineering and Medicine in Biology Society, pp1096-9.

[14] El Fakhri, G., et al. (2005). Quantitative dynamic cardiac Rb-82 PET using generalized factor and compartment analyses. Journal of Nuclear Medicine, 46(8), 1264-1271.

[15] Lortie, M., et al. (2007). Quantification of myocardial blood flow with Rb-82 dynamic PET imaging. European journal of nuclear medicine and molecular imaging, 34(11), 1765-1774.

[16] Uren, N.G., et al. (1994), Relation between myocardial blood flow and the severity of coronary-artery stenosis. N Engl J Med, 330(25), 1782-8.

[17] Parkash, R., et al. (2004). Potential utility of rubidium 82 PET quantification in patients with 3-vessel coronary artery disease. Journal of Nuclear Cardiology, 11(4), 440-449.

[18] Lodge, M. and Bengel F. (2007). Methodology for quantifying absolute myocardial perfusion with PET and SPECT. Current Cardiology Reports, 9(2), 121-128.

[19] Dayanikli, F., et al. (1994). Early detection of abnormal coronary flow reserve in asymptomatic men at high risk for coronary artery disease using positron emission tomography. Circulation, 90(2), 808-17.

[20] Higuchi, T., et al. (2007). Effect of the angiotensin receptor blocker Valsartan on coronary microvascular flow reserve in moderately hypertensive patients with stable coronary artery disease. Microcirculation, 14(8), 805-812.

[21] Yoshinaga, K., et al. (2006). Effect of exercise training on myocardial blood flow in patients with stable coronary artery disease. American Heart Journal, 151(6), 1324.e11-1324.e18.

[22] Tsukamoto, T., et al. (2006). Myocardial flow reserve is influenced by both coronary artery stenosis severity and coronary risk factors in patients with suspected coronary artery disease. European journal of nuclear medicine and molecular imaging, 33(10), 1150-1156.

[23] Pitkanen, O.P., et al. (1996). Coronary flow reserve is impaired in young men with familial hypercholesterolemia. Journal of the American College of Cardiology, 28(7), 1705-1711.

[24] Campisi, R., et al. (1998). Effects of long-term smoking on myocardial blood flow, coronary vasomotion, and vasodilator capacity. Circulation, 98(2), 119-125.

[25] Di Carli, M., et al. (1999). Effects of autonomic neuropathy on coronary blood flow in patients with diabetes mellitus. Circulation, 100(8), 813-819.

[26] Kaufmann, P.A., et al. (2000). Coronary heart disease in smokers - Vitamin C restores coronary microcirculatory function. Circulation, 102(11), 1233-1238.

[27] Momose, M., et al. (2002). Dysregulation of coronary microvascular reactivity in asymptomatic patients with type 2 diabetes mellitus. European journal of nuclear medicine and molecular imaging, 29(12), 1675-1679.

[28] Di Carli, M.F., et al. (2002). Coronary vascular dysfunction in premenopausal women with diabetes mellitus. American Heart Journal, 144(4), 711-718.

[29] Kjaer, A., et al. (2003). Dipyridamole, cold pressor test, and demonstration of endothelial dysfunction: A PET study of myocardial perfusion in diabetes. Journal of Nuclear Medicine, 44(1), 19-23.

[30] Schindler, T.H., et al. (2004). Chronic inflammation and impaired coronary vasoreactivity in patients with coronary risk factors. Circulation, 110(9), 1069-1075.

[31] Bengel, F.M., et al. (2005). Effects of nateglinide on myocardial microvascular reactivity in Type 2 diabetes mellitus - a randomized study using positron emission tomography. Diabetic Medicine, 22(2), 158-163.

[32] Lautamaki, R., et al. (2006). Insulin improves myocardial blood flow in patients with type 2 diabetes and coronary artery disease. Diabetes, 55(2), 511-516.

[33] Schindler, T.H., et al. (2005). Positron emission tomography-measured abnormal responses of myocardial blood flow to sympathetic stimulation are associated with the risk of developing cardiovascular events. Journal of the American College of Cardiology, 45(9), 1505-1512.

[34] Schindler, T.H., et al. (2003). Regional myocardial perfusion defects during exercise, as assessed by three dimensional integration of morphology and function, in relation to abnormal endothelium dependent vasoreactivity of the coronary microcirculation. Heart, 89(5), 517-526.

[35] Schachinger, V., M.B. Britten, and Zeiher, A.M. (2000). Prognostic impact of coronary vasodilator dysfunction on adverse long-term outcome of coronary heart disease. Circulation, 101(16), 1899-1906.

[36] Camici, P.G. and Crea, F. (2007). Coronary Microvascular Dysfunction. New England Journal of Medicine, 356(8), 830-840.

[37] Guethlin, M., et al. (1999). Delayed response of myocardial flow reserve to lipid-lowering therapy with fluvastatin. Circulation, 99(4), 475-81.

[38] Huggins, G.S., et al. (1998). Effects of short-term treatment of hyperlipidemia on coronary vasodilator function and myocardial perfusion in regions having substantial impairment of baseline dilator reverse. Circulation, 98(13), 1291-6.

[39] Bengel, F.M., et al. (2009). Cardiac Positron Emission Tomography. Journal of the American College of Cardiology, 54(1), 1-15.

[40] Tsoumpas, C., F.E. Turkheimer, and Thielemans, K. (2008). A survey of approaches for direct parametric image reconstruction in emission tomography. Med Phys, 35(9), 3963-71.

[41] Rahmim, A., J. Tang, and Zaidi, H. (2009). Four-dimensional (4D) image reconstruction strategies in dynamic PET: beyond conventional independent frame reconstruction. Med Phys, 36(8), 3654-70.

[42] Wang, G. and Qi, J. (in press, 2013). Direct Estimation of Kinetic Parametric Images for Dynamic PET Theranostics.

[43] Tang, J., et al. (2011). Direct 4D parametric image reconstruction for dynamic cardiac PET imaging. J. Nuc. Med., 51 (suppl. 1), 1996.

[44] Rahmim, A., et al. (2011). Use of optimization transfer for enhanced direct 4D parametric imaging in myocardial perfusion PET. J. Nuc. Med., 51 (suppl. 1), 265.

[45] Mohy-ud-Din, H., et al. (2011). Comparison of ordered subset implementations for EM, preconditioned steepest ascent (PSA) and conjugate gradient (PCG) optimization tasks in PET image reconstruction. J. Nucl. Med., 51 (suppl. 1), 1997.

[46] Weinberg, I.N., et al. (1988). Validation of PET-Acquired Input Functions for Cardiac Studies. J.Nucl.Med., 29(2), 241-247.

[47] Yan, J.H. and Yu, J. (2006). Emission image reconstruction based on incremental optimization transfer algorithm. First International Multi-Symposiums on Computer and Computational Sciences (IMSCCS 2006), Proceedings, Vol 2, 266-269

[48] Ahn, S., et al. (2006). Convergent incremental optimization transfer algorithms: Application to tomography. IEEE Transactions on Medical Imaging, 25(3), 283-296.

[49] Ahn, S.T., et al. (2004). Incremental optimization transfer algorithms: Application to transmission tomography. 2004 IEEE Nuclear Science Symposium Conference Record, Vols 1-7, 2835-2839

[50] Jacobson, M. and Fessler, J.A. (2002). Simultaneous estimation of attenuation and activity images using optimization transfer. 2001 Ieee Nuclear Science Symposium, Conference Records, Vols 1-4, 2085-2089

[51] Lange, K., Hunter, D.R.and Yang, I. (2000). Optimization transfer using surrogate objective functions. Journal of Computational and Graphical Statistics, 9(1), 1-20.

[52] Wang, G. and Qi, J. (2010). Acceleration of the direct reconstruction of linear parametric images using nested algorithms. Phys Med Biol, 55, 1505-1517.

[53] Wang, G.B. and Qi, J.Y. (2009). Generalized Algorithms for Direct Reconstruction of Parametric Images From Dynamic PET Data. IEEE Transactions on Medical Imaging, 28(11), 1717-1726.

[54] Wang, G.B. and Qi, J.Y. (2012). An Optimization Transfer Algorithm for Nonlinear Parametric Image Reconstruction From Dynamic PET Data. IEEE Transactions on Medical Imaging, 31(10), 1977-1988.

[55] Hudson, H.M. and Larkin, R.S. (1994). Accelerated image reconstruction using ordered subsets of projection data. IEEE Trans Med Imaging, 13(4), 601-609.

[56] Shepp, L.A. and Vardi, Y. (1982). Maximum likelihood reconstruction for emission tomography. IEEE Trans Med Imaging, 1, 113-122.

[57] Lange, K. and Carson, R. (1984). EM reconstruction algorithms for emission and transmission tomography. J Comput Assist Tomogr, 8(2), 306-316.

[58] Vardi, Y., Shepp, L.A. and Kaufman, L. (1985). A Statistical-Model for Positron Emission Tomography. Journal of the American Statistical Association, 80(389), 8-20.

[59] Lange, K., M. Bahn, and Little, R. (1987). A theoretical study of some maximum likelihood algorithms for emission and transmission tomography. IEEE Transactions on Medical Imaging, MI-6, 106-114.

[60] Kaufman, L. (1987). Implementing and Accelerating the Em Algorithm for Positron Emission Tomography. IEEE Transactions on Medical Imaging, 6(1), 37-51.

[61] Nocedal, J. and Wright, S.J. (2006). Numerical Optimization (2nd ed.). Springer.

[62] Segars, W.P., et al., Realistic CT simulation using the 4D XCAT phantom. 2008, AAPM. p. 3800-3808.

[63] Kemp, B.J., et al. (2006). NEMA NU 2-2001 performance measurements of an LYSO-based PET/CT system in 2D and 3D acquisition modes. J Nucl Med, 47(12), 1960-7.

[64] Tang, J., et al. (2009). Optimization of Rb-82 PET acquisition and reconstruction protocols for myocardial perfusion defect detection Phys Med Biol, 54, 3161-71.

[65] Kotasidis, F.A., et al. (2011). Impact of erroneous kinetic model formulation in Direct 4D image reconstruction. in Nuclear Science Symposium and Medical Imaging Conference (NSS/MIC), 2011 IEEE.

[66] Kotasidis, F.A., et al. (2012). Application of adaptive kinetic modelling for bias propagation reduction in direct 4D image reconstruction. in Nuclear Science Symposium and Medical Imaging Conference (NSS/MIC), 2012 IEEE.

[67] Tahari, A.K., Bravo, P.E., Rahmim, A., Bengel, F.M., Szabo, Z. (2013). Initial human experience with Rubidium-82 renal PET/CT imaging. Journal of Medical Imaging and Radiation Oncology.

[68] Rahmim, A. and Zaidi, H. (2008). PET versus SPECT: strengths, limitations and challenges. Nucl Med Commun, 29(3), 193-207.

[69] Iida, H., et al. (1988). Measurement of Absolute Myocardial Blood-Flow with (H2o)-O-15 and Dynamic Positron-Emission Tomography - Strategy for Quantification in Relation to the Partial-Volume Effect. Circulation, 78(1), 104-115.

[70] Iida, H., et al. (1991). Myocardial Tissue Fraction - Correction for Partial Volume Effects and Measure of Tissue Viability. Journal of Nuclear Medicine, 32(11), 2169-2175.

[71] Hutchins, G.D., Caraher, J.M. and Raylman, R.R. (1992). A Region of Interest Strategy for Minimizing Resolution Distortions in Quantitative Myocardial Pet Studies. Journal of Nuclear Medicine, 33(6), 1243-1250.

[72] Hutchins, G.D., et al. (1990). Noninvasive quantification of regional blood flow in the human heart using N-13 ammonia and dynamic positron emission tomographic imaging. J Am Coll Cardiol, 15(5), 1032-42.

[73] Muzik, O., et al. (1993). Validation of Nitrogen-13-Ammonia Tracer Kinetic-Model for Quantification of Myocardial Blood-Flow Using Pet. Journal of Nuclear Medicine, 34(1), 83-91.

[74] van den Hoff, J., et al. (2001). Acetate as a quantitative perfusion tracer in myocardial PET. Journal of Nuclear Medicine, 42(8), 1174-1182.

[75] Nuyts, J., et al. (1996). Three-dimensional correction for spillover and recovery of myocardial PET images. Journal of Nuclear Medicine, 37(5), 767-774.

[76] Pretorius, P.H. and King, M.A. (2009). Diminishing the impact of the partial volume effect in cardiac SPECT perfusion imaging. Medical Physics, 36(1), 105-115.

[77] Du, Y., et al. (2013). Compensation for spill-in and spill-out partial volume effects in cardiac PET imaging. Journal of Nuclear Cardiology, 20(1), 84-98.

[78] Dumouchel, T., et al. (2012). A three-dimensional model-based partial volume correction strategy for gated cardiac mouse PET imaging. Physics in Medicine and Biology, 57(13), 4309-4334.

[79] Erlandsson, K., et al. (2012). A review of partial volume correction techniques for emission tomography and their applications in neurology, cardiology and oncology. Physics in Medicine and Biology, 57(21), R119-R159.

[80] Rahmim, A., et al. (2008). Analytic system matrix resolution modeling in PET: an application to Rb-82 cardiac imaging. Phys Med Biol, 53(21), 5947-65.

[81] Le Meunier, L., et al. (2011). Motion frozen F-18-FDG cardiac PET. Journal of Nuclear Cardiology, 18(2), 259-266.

[82] Le Meunier, L., et al. (2010). Enhanced definition PET for cardiac imaging. Journal of Nuclear Cardiology, 17(3), 414-426.

[83] Blinder, S.A., Dinelle, K., Sossi, V. (2012). Scanning rats on the high resolution research tomograph (HRRT): A comparison study with a dedicated micro-PET. Med Phys, 39(8), 5073-83.

[84] Rahmim, A., Qi, J., Sossi, V. (2013). Resolution modeling in PET imaging: Theory, practice, benefits and pitfalls. Med Phys, 40, 064301.